THE ASTROPHYSICAL JOURNAL, 466:549–560, 1996 July 20

HIGH CORONAL ELECTRON DENSITIES IN A SOLAR FLARE FROM Fe XXI AND Fe XXII X-RAY LINE MEASUREMENTS

K. J. H. PHILLIPS,[1] A. K. BHATIA,[2] H. E. MASON,[3] AND D. M. ZARRO[4]

Received 1995 August 21; accepted 1996 February 5

ABSTRACT

New calculations of the intensities of the Fe XXI $2p^2$–$2p4l$ X-ray lines using the distorted wave method are described and compared with observations made by a crystal spectrometer on the *Solar Maximum Mission* about 6 minutes after the peak of a very intense flare. The comparison enables the electron density of the flare to be derived, the value being about 2 or 3×10^{12} cm^{-3}. Some nearby Fe XXII X-ray lines, scanned 1 minute after flare peak, give an even higher value, 10^{13} cm^{-3}. This is the first time corroborated values of such high densities have been obtained from ions emitted at temperatures as high as ~10 MK. They imply very rapid radiation cooling rates and have other important consequences for flare models.

Subject headings: atomic processes — Sun: corona — Sun: flares — Sun: X-rays, gamma rays

1. INTRODUCTION

The accurate estimation of electron densities N_e in hot soft X-ray flare plasmas is an important issue in solar physics, since different models for the formation of the plasma predict different densities, while cooling mechanisms such as radiation depend critically on the value of N_e. Approximate values of N_e may be obtained from X-ray flare images, as was done extensively with *Skylab* data (e.g., Pallavicini, Serio, & Vaiana 1977). By assuming an isothermal plasma and with a measured flux and emissivity appropriate to the spectral region calculated from atomic data, the emission measure $\langle N_e^2 V \rangle$ may be obtained, which, when combined with the volume V estimated from the image, gives N_e. This and similar indirect methods assume that the emitting plasma fills the instrumental field of view, i.e., that the filling factor is unity. Flare models suggest that this may not be true. If, for example, flares result from a tearing-mode instability (e.g., Spicer 1977), there may be several very small emitting volumes, identifiable with magnetic "islands," within the field of view. Again, in the DC electric field model of Benka & Holman (1994) (see also Holman & Benka 1992; Zarro, Mariska, & Dennis 1995), a large number of tiny current channels exist, aligned with the magnetic field. In each case, the emitting regions may well be beyond the spatial resolution of any imaging spacecraft instrument. Some observational evidence of small filling factors has been provided by images taken with the soft X-ray telescope (SXT) on the *Yohkoh* spacecraft (Acton et al. 1992; Feldman et al. 1994) showing that the main emitting region of a flare is frequently at most the size of a single SXT pixel size, about 1800 × 1800 km.

Certain spectral line ratios in high-temperature ions offer a direct means of finding N_e, so that the filling factor does not have to be known. With N_e determined in this way, and a value for emission measure $\langle N_e^2 V \rangle$, the above argument can be applied in reverse to find the emitting volume V. There are a few X-ray lines in the 1–20 Å range that are density sensitive but in general only for $N_e \gtrsim 10^{12}$ cm^{-3}. Such a value is somewhat higher than most flare density estimates from *Skylab* data, though Underwood et al. (1978) obtained $N_e \approx 10^{12}$ cm^{-3} for a compact flare. Examples of such lines include those due to $n = 2$–3 transitions in O-like Fe (Fe XIX) to B-like Fe (Fe XXII), occurring in the 11–13 Å range. These ions, which are formed at temperatures of about 10 MK, all have two or more fine-structure levels within their ground configurations. For low densities ($N_e \lesssim 3 \times 10^{11}$ cm^{-3}), the ions are almost entirely in the ground level, but for higher densities excited levels of the ground configuration are significantly populated (Mason et al. 1979; Mason & Storey 1980; Loulergue et al. 1985). This leads to the excitation of certain lines that would not normally occur in the low-density limit. Values of N_e equal to or less than the low-density limit were deduced from the apparent absence of such lines due to Fe XXI and Fe XXII in spectral scans made with the Flat Crystal Spectrometer (FCS) on the *Solar Maximum Mission* (*SMM*) during the decay of an M1 flare (Phillips et al. 1982). A similar result for the decay phase of other flares was obtained from density-sensitive inner-shell $1s$–$2p$ lines at around 1.9 Å of these same ions (Phillips et al. 1983) observed by the Bent Crystal Spectrometer (BCS) on *SMM*. In this case, dielectronic recombination is the chief way of forming the upper levels of such lines, and the density sensitivity arises because of the density-dependent populations of the recombining ion's ground-configuration levels.

The intensity ratio of the forbidden ($1s^2\,{}^1S_0$–$1s2s\,{}^3S_1$) to intercombination ($1s^2\,{}^1S_0$–$1s2p\,{}^3P_1$) lines emitted by He-like ions are also N_e dependent (Gabriel & Jordan 1969), but the ions of interest for solar coronal plasmas, from O VII to Mg XI ($Z = 8$–12) are formed at temperatures much lower than the maximum values (about 20 MK) attained in flares (e.g., Mg XI lines are emitted at 6 MK—see Mewe, Gronenschild, & van den Oord 1985). For each helium-like ion, there is a critical density N_c above which the intercombination line increases in intensity at the expense of the forbidden line: for O, $N_c \approx 3 \times 10^{10}$ cm^{-3}, and for Mg, $N_c \approx 10^{12}$ cm^{-3}. Density variations during solar flares with N_e increasing to 10^{12} cm^{-3} at peak intensity and decreasing thereafter have been measured from O VII lines (McKenzie et al. 1980) and Ne IX lines (Wolfson

[1] Space Science Department, Rutherford Appleton Laboratory, Chilton, Didcot, Oxon OX11 0QX, UK.
[2] Code 680, NASA Goddard Space Flight Center, Greenbelt, MD 20771.
[3] Department of Applied Mathematics and Theoretical Physics, Cambridge University, Silver Street, Cambridge CB3 9EW, UK.
[4] Applied Research Corporation, NASA Goddard Space Flight Center, Greenbelt, MD 20771.

et al. 1983; Bhatia et al. 1989). Linford & Wolfson (1988) and Linford, Lemen, & Strong (1991) have analyzed FCS measurements of Mg XI line intensities in a compact flare which imply values of N_e as high as 5×10^{12} cm^{-3}.

A spectral scan in the 7.3–10.0 Å range with the FCS instrument during an intense (M4.5) flare on 1985 July 2 revealed several lines, many quite intense, either not previously observed or not identified. Fawcett et al. (1987), in a discussion of these observations, showed these lines to be mostly due to $2s^2\,2l$–$2s^2\,4l'$ transitions in ions from Fe XIX to Fe XXII. As with corresponding $n = 2$–3 lines, a density dependence is expected for lines of, e.g., Fe XXI and Fe XXII. Distorted wave calculations of collision strengths and relative intensities as a function of N_e by Mason & Storey (1980) already exist for the Fe XXII lines, enabling comparison with the observations.

For the case of the Fe XXI $2p^2$–$2p4l$ lines, accurate collision strengths have not been available until now, preventing this potentially useful flare density diagnostic from being exploited. In this work, we report on new distorted wave calculations of the collisional excitation rates for the Fe XXI lines in question and resulting line intensities as a function of N_e. These are compared with the FCS observations to derive N_e. This value is discussed in the context of the value from the Fe XXII lines and density limits from inner shell $1s$–$2p$ Fe XX lines at 1.90 Å observed with the BCS. The implications for flare cooling mechanisms and energy balance and constraints imposed on certain flare models are then discussed.

2. Fe XXI ATOMIC DATA AND SYNTHETIC SPECTRA

The Fe XXI lines of this study are due to transitions between the fine-structure levels making up the $1s^2\,2s^2\,2p^2$ ground configuration and the $1s^2\,2s^2\,2p\,4l$, $l = s$, d, upper configuration. The fine-structure levels of the ground configuration are (in order of increasing energy) $^3P_0$, $^3P_1$, $^3P_2$, $^1D_2$, and $^1S_0$. Excitation of the upper levels proceeds by electron collisions of Fe XXI ions in any of the ground configuration levels, with a small contribution made by proton collisions.

First we ran the University College London SUPERSTRUCTURE code (Eissner, Jones, & Nussbaumer 1974), which computes the energy levels and radiative data in intermediate coupling, allowing for configuration interaction. It assumes a scaled Thomas-Fermi potential for the one-electron radial orbitals, the scaling parameters used for Fe XXI being $\lambda_s = 1.3518$, $\lambda_p = 1.2041$, and $\lambda_d = 1.2960$. Spin-orbit and spin-spin interactions and other relativistic corrections are treated as perturbations to the Hamiltonian. Table 1 gives level assignments and energies (cm^{-1}) for all levels of the $2s^2\,2p^2$, $2s2p^3$, $2p^4$, $2s^2\,2p4l$, and (for completeness) $2s^2\,2p5l$ configurations ($l = s$, d).

An electron scattering program, DSTWAV, was then run, based on the distorted wave approximation with scaled Thomas-Fermi potential for the one-electron orbitals (Eissner & Seaton 1972). The $\boldsymbol{R}$-matrices were calculated in LS coupling, with the program JAJOM (Saraph 1972) being used to transform these into pair-coupled collision strengths with term-coupling coefficients from SUPERSTRUCTURE. For higher partial wave values ($l > 18$) of the colliding electron, the Coulomb-Bethe approximation was used, following Burgess & Sheorey (1974). Proton excitation was included in the calculation, using the semiclassical Coulomb excitation approximation of Kastner & Bhatia (1979). Table 2 gives, for transitions between the levels i and j indicated (using the notation of Table 1), oscillator strengths gf_{ij}, transition rates A_{ji} (s^{-1}), and total electron collision strengths Ω_{ij} for incident electron energies equal to 110, 220, and 330 ryd. Transitions between all the levels of Table 1 are included if the collision strength at one of the three energies exceeded 0.0001. Transitions between the $2s^2\,2p^2$ and $2s2p^3$ levels are given in Table 2, though their intensities are not considered in this paper. This allows comparison with atomic data calculated by Mason et al. (1979), which in fact show a very close correspondence. (The level notation of Mason et al. is the same as that of Table 1 for levels 1–15.)

The collision strengths Ω_{ij} in Table 2 were integrated over Maxwellian distributions to obtain excitation rate coeffi-

TABLE 1

CALCULATED Fe XXI ENERGY LEVELS

Index	Configuration	Level	Energy (cm^{-1})
1.....	$2s^2\,2p^2$	$^3P_0$	0
2.....		$^3P_1$	72,594
3.....		$^3P_2$	116,154
4.....		$^1D_2$	243,195
5.....		$^1S_0$	363,007
6.....	$2s\,2p^3$	$^5S_2$	472,682
7.....		$^3D_1$	773,432
8.....		$^3D_2$	774,273
9.....		$^3D_3$	803,775
10.....		$^3P_0$	910,145
11.....		$^3P_1$	920,500
12.....		$^3P_2$	939,196
13.....		$^3S_1$	1,102,382
14.....		$^1D_2$	1,135,551
15.....		$^1P_1$	1,266,801
16.....	$2p^4$	$^3P_2$	1,652,140
17.....		$^3P_0$	1,740,239
18.....		$^3P_1$	1,744,092
19.....		$^1D_2$	1,830,225
20.....		$^1S_0$	2,059,487
21.....	$2s^2\,2p4s$	$^3P_0$	10,420,364
22.....		$^3P_1$	10,423,667
23.....		$^3P_2$	10,534,262
24.....		$^1P_1$	10,541,942
25.....	$2s^2\,2p4d$	$^3F_2$	10,584,061
26.....		$^1D_2$	10,601,813
27.....		$^3F_3$	10,602,392
28.....		$^3D_1$	10,607,688
29.....		$^3F_4$	10,701,512
30.....		$^3D_2$	10,702,437
31.....		$^3D_3$	10,709,804
32.....		$^3P_1$	10,716,288
33.....		$^1P_2$	10,716,363
34.....		$^3P_0$	10,716,855
35.....		$^1F_3$	10,734,402
36.....		$^1P_1$	10,736,851
37.....	$2s^2\,2p5s$	$^3P_0$	11,625,443
38.....		$^3P_1$	11,626,909
39.....	$2s^2\,2p5d$	$^3F_2$	11,707,274
40.....		$^1D_2$	11,714,849
41.....		$^3F_3$	11,716,379
42.....		$^3D_1$	11,717,986
43.....	$2s^2\,2p5s$	$^3P_2$	11,739,982
44.....		$^1P_1$	11,742,830
45.....	$2s^2\,2p5d$	$^3F_4$	11,823,124
46.....		$^3D_2$	11,823,214
47.....		$^3D_3$	11,826,334
48.....		$^3P_1$	11,829,349
49.....		$^3P_2$	11,829,429
50.....		$^3P_0$	11,829,646
51.....		$^3F_3$	11,837,406
52.....		$^1P_1$	11,838,880

TABLE 2

ATOMIC DATA FOR Fe XXI ULTRAVIOLET AND (n = 2–4, 5) X-RAY LINES

Transition[a] (i–j)	gf_{ij}	A_{ji} (s^{-1})	COLLISION STRENGTHS FOR ENERGIES		
			110 ryd	220 ryd	330 ryd
1–2	...	6.21(3)	0.0063	0.0031	0.0018
1–3	...	7.51(−1)	0.0114	0.0104	0.0101
1–4	...	2.74(−1)	0.0012	0.0006	0.0004
1–5	...	...	0.0001	0.0001	0.0000
1–6	...	...	0.0014	0.0007	0.0004
1–7	9.16(−2)	1.22(10)	0.2535	0.2961	0.3228
1–8	...	...	0.0012	0.0006	0.0004
1–11	2.36(−2)	4.45(09)	0.0533	0.0614	0.0668
1–13	3.80(−2)	1.03(10)	0.0652	0.0765	0.0838
1–22	1.04(−2)	2.52(11)	0.0002	0.0003	0.0004
1–28	2.55(−1)	6.37(12)	0.0091	0.0150	0.0187
1–42	9.07(−2)	2.77(12)	0.0030	0.0050	0.0063
2–3	...	8.64(02)	0.0248	0.0186	0.0163
2–4	...	1.50(04)	0.0116	0.0073	0.0058
2–5	...	1.28(05)	0.0015	0.0006	0.0004
2–6	1.58(−3)	3.38(07)	0.0140	0.0139	0.0141
2–7	7.48(−3)	8.17(08)	0.0248	0.0280	0.0302
2–8	1.52(−1)	9.98(09)	0.4807	0.5598	0.6087
2–9	...	...	0.0011	0.0006	0.0003
2–10	5.05(−2)	2.36(10)	0.1276	0.1478	0.1609
2–11	1.04(−1)	1.67(10)	0.2576	0.2999	0.3269
2–12	4.51(−3)	4.52(08)	0.0122	0.0134	0.0142
2–13	1.17(−1)	2.75(10)	0.2205	0.2581	0.2823
2–14	2.69(−3)	4.06(08)	0.0063	0.0064	0.0066
2–15	1.66(−2)	5.27(09)	0.0262	0.0303	0.0331
2–21	9.88(−3)	7.06(11)	0.0001	0.0003	0.0004
2–23	2.11(−2)	3.07(11)	0.0004	0.0006	0.0008
2–25	6.15(−3)	9.07(10)	0.0016	0.0010	0.0010
2–26	3.30(−1)	4.88(12)	0.0132	0.0202	0.0250
2–28	4.01(−2)	9.91(11)	0.0028	0.0027	0.0031
2–30	1.29(−1)	1.95(12)	0.0051	0.0077	0.0095
2–32	1.55(−1)	3.91(12)	0.0057	0.0091	0.0114
2–33	5.93(−2)	8.97(11)	0.0029	0.0037	0.0044
2–34	6.66(−2)	5.03(12)	0.0024	0.0039	0.0049
2–40	1.32(−1)	2.39(12)	0.0046	0.0073	0.0091
2–42	1.34(−2)	4.05(11)	0.0011	0.0009	0.0010
2–46	4.18(−2)	7.69(11)	0.0016	0.0024	0.0029
2–48	5.71(−2)	1.76(12)	0.0019	0.0032	0.0040
2–49	2.19(−2)	4.03(11)	0.0012	0.0013	0.0016
2–50	2.42(−2)	2.23(12)	0.0008	0.0013	0.0017
3–4	...	1.45(04)	0.0337	0.0265	0.0240
3–5	...	5.13(04)	0.0044	0.0035	0.0033
3–6	1.93(−3)	3.28(07)	0.0196	0.0196	0.0199
3–7	7.10(−4)	6.81(07)	0.0029	0.0031	0.0033
3–8	1.50(−4)	8.64(06)	0.0028	0.0018	0.0014
3–9	1.50(−1)	6.76(09)	0.4913	0.5693	0.6180
3–10	...	...	0.0005	0.0002	0.0001
3–11	2.22(−2)	3.19(09)	0.0602	0.0688	0.0746
3–12	2.70(−1)	2.17(10)	0.6160	0.7166	0.7805
3–13	3.05(−1)	6.60(10)	0.6155	0.7187	0.7848
3–14	6.10(−2)	8.45(09)	0.1175	0.1369	0.1495
3–15	6.01(−4)	1.77(08)	0.0025	0.0019	0.0017
3–22	1.84(−2)	4.35(11)	0.0005	0.0006	0.0008
3–23	3.58(−2)	5.18(11)	0.0007	0.0011	0.0015
3–25	4.12(−2)	6.02(11)	0.0041	0.0034	0.0036
3–26	2.92(−2)	4.29(11)	0.0031	0.0026	0.0027
3–27	3.50(−1)	3.67(12)	0.0151	0.0215	0.0265
3–28	3.87(−3)	9.46(10)	0.0012	0.0007	0.0007
3–30	4.85(−2)	7.25(11)	0.0040	0.0035	0.0038
3–31	5.36(−1)	5.73(12)	0.0201	0.0318	0.0397
3–32	7.02(−2)	1.75(12)	0.0033	0.0044	0.0053
3–33	2.31(−1)	3.46(12)	0.0094	0.0141	0.0174
3–38	6.32(−3)	1.86(11)	0.0002	0.0002	0.0003
3–39	1.70(−2)	3.04(11)	0.0018	0.0013	0.0014
3–40	1.37(−2)	2.46(11)	0.0014	0.0010	0.0010
3–41	1.52(−1)	1.95(12)	0.0061	0.0088	0.0109
3–46	1.87(−2)	3.41(11)	0.0017	0.0014	0.0014

TABLE 2—*Continued*

Transition[a] (i–j)	gf_{ij}	A_{ji} (s^{-1})	Collision Strengths for Energies 110 ryd	220 ryd	330 ryd
3–47	1.79(−1)	2.34(12)	0.0063	0.0101	0.0126
3–48	2.54(−2)	7.73(11)	0.0012	0.0015	0.0018
3–49	8.15(−2)	1.49(12)	0.0032	0.0048	0.0059
4–5	...	1.16(01)	0.0225	0.0239	0.0246
4–6	1.70(−4)	1.19(06)	0.0031	0.0030	0.0030
4–7	3.28(−3)	2.05(08)	0.0176	0.0189	0.0198
4–8	1.03(−3)	3.88(07)	0.0083	0.0073	0.0070
4–9	3.39(−2)	1.01(09)	0.1508	0.1710	0.1836
4–10	...	...	0.0001	0.0001	0.0000
4–11	2.83(−3)	2.88(08)	0.0106	0.0115	0.0122
4–12	3.13(−3)	2.02(08)	0.0140	0.0136	0.0138
4–13	1.33(−3)	2.18(08)	0.0035	0.0391	0.0419
4–14	4.68(−1)	4.97(10)	1.076	1.256	1.370
4–15	3.10(−1)	7.22(10)	0.5992	0.6962	0.7595
4–24	3.35(−2)	7.90(11)	0.0006	0.0010	0.0015
4–25	1.57(−2)	2.23(11)	0.0012	0.0012	0.0013
4–26	1.63(−2)	2.33(11)	0.0010	0.0011	0.0013
4–27	4.37(−2)	4.47(11)	0.0025	0.0029	0.0034
4–30	7.56(−2)	1.10(12)	0.0053	0.0057	0.0066
4–31	1.70(−2)	1.78(11)	0.0046	0.0023	0.0020
4–32	1.70(−2)	4.14(11)	0.0020	0.0014	0.0015
4–33	1.45(−1)	2.12(12)	0.0075	0.0093	0.0111
4–35	9.48(−1)	9.94(12)	0.0344	0.0563	0.0706
4–39	4.71(−3)	8.26(10)	0.0005	0.0004	0.0004
4–41	2.94(−2)	3.68(11)	0.0013	0.0018	0.0022
4–46	2.64(−2)	4.71(11)	0.0021	0.0020	0.0022
4–49	5.43(−2)	9.73(11)	0.0030	0.0034	0.0040
4–51	3.57(−1)	4.57(12)	0.0118	0.0200	0.0252
5–7	1.40(−3)	5.23(07)	0.0090	0.0104	0.0112
5–10	...	...	0.0006	0.0003	0.0002
5–11	2.48(−3)	1.72(08)	0.0125	0.0134	0.0140
5–12	...	...	0.0016	0.0008	0.0005
5–13	5.87(−3)	7.13(08)	0.0176	0.0204	0.0221
5–15	1.04(−1)	1.90(10)	0.2332	0.2740	0.2997
5–28	8.99(−3)	2.10(11)	0.0004	0.0006	0.0007
5–36	2.37(−1)	5.67(12)	0.0085	0.0143	0.0180
5–42	6.09(−3)	1.75(11)	0.0002	0.0004	0.0005
5–52	8.94(−2)	2.62(12)	0.0029	0.0051	0.0064

NOTE.—Numbers in parentheses are powers of 10.
[a] Level notation is that of Table 1.

cients at electron temperatures T_e. Fractional level populations $n_j = N_j/N_T$ (N_j = number density of level j, N_T the sum of number densities of all Fe XXI levels) were obtained by solving the set of coupled rate equations for different values of electron density N_e.

The populations of the five ground-configuration ($2s^2\,2p^2$) levels of Fe XXI are plotted in Figure 1 for $N_e = 10^{10}$–10^{14} cm^{-3}. A temperature T_e of 10 MK was used in these calculations, very close to the temperature of maximum emissivity for the $n = 2$–4 X-ray lines. There is a dependence of level population on temperature in the range 8–12 MK, but this amounts to less than 15%. In Figure 1 we show also the level populations of Conlon, Keenan, & Aggarwal (1992), obtained from ***R***-matrix calculations, which are likely to be more accurate than ours although they are only for electron densities of 10^{12} cm^{-3} and above. Also, while Conlon et al. consider the 20 levels of the $2s^2\,2p^2$, $2s2p^3$, and $2p^4$ configurations and the ultraviolet transitions between these levels, we include much higher levels and X-ray transitions. As can be seen from Figure 1, our calculated populations are generally within a few percent of those of Conlon et al. (1992). They are also very similar to those of Mason et al. (1979).

The X-ray lines we consider are all optically thin, so that the relative intensities (in photon units, not energy units) are given by $I_{ij} = n_j A_{ji}$. Table 3 gives these values, relative to the line with transition 1–28 (the most intense), at a density $N_e = 10^{10}$ cm^{-3}, as well as theoretical wavelengths. Relative intensities are given for $n = 2$–4 and $n = 2$–5 lines with values of log $N_e = 10$, 11, 12, and 13.

The spectral region 9.4–9.8 Å, which includes all the intense Fe XXI lines in the $2p^2$–$2p4l$ ($l = s$, d) arrays, was synthesized using the intensity ratios given in Table 3. The method is described by Phillips et al. (1993). Briefly, theoretical spectra were formed by giving each line a Voigt profile that describes the chief broadening mechanisms appropriate for the FCS channel viewing the Fe XXI lines, viz., the crystal rocking curve (approximately Lorentzian in shape) and thermal Doppler broadening (Gaussian shape). For the latter, we assumed electron and ion temperatures to be equal on the basis of the equilibrium times given by Spitzer (1962), which are at most only a few seconds for particle densities of 10^{11} cm^{-3} or greater and temperatures of $\sim$10 MK. Figure 2 shows synthetic spectra in this range for three densities, $N_e = 10^{11}$, 10^{12}, and 10^{13} cm^{-3} (there are only very small differences between the spectra for

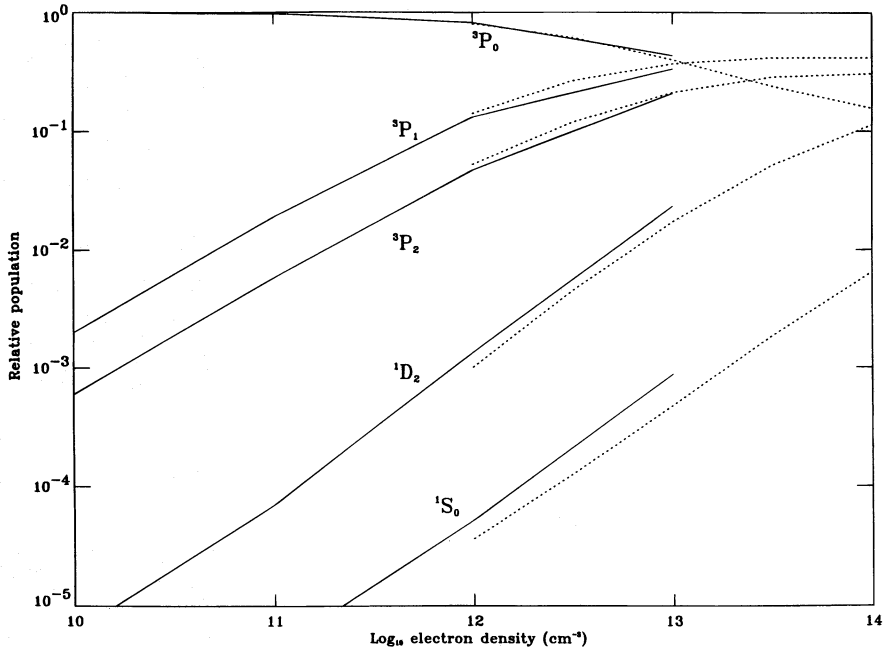

FIG. 1.—Populations of the five levels of the Fe XXI ground configuration $2s^2\,2p^2$ from the present calculations (*solid lines*) compared with those of Conlon et al. (1992) (*dashed lines*), plotted against electron density N_e (log scale) at a temperature of 10 MK.

$N_e = 10^{10}$ and 10^{11} cm^{-3}). For densities above 10^{12} cm^{-3}, there is a considerable increase in the intensity of lines at 9.4396 Å (transition 3–31), 9.4974 Å (2–26), and 9.5363 Å (3–27) (wavelengths are theoretical values). The intensity increases reflect the fact that these lines are excited primarily from excited levels $^3P_1$ (level 2 in the notation of Table 1) or $^3P_2$ (level 3) of the $2s^2\,2p^2$ array, which are only significantly populated when $N_e \gtrsim 10^{12}$ cm^{-3}.

3. THE OBSERVATIONS

The FCS instrument on *SMM* and analysis of the data have been described in detail (Acton et al. 1980; Phillips et al. 1982). The FCS was a finely collimated (14″ × 14″) scanning Bragg crystal spectrometer with seven crystals attached to a rotatable shaft driven by one of two drive-encoder units at either end. Radiation diffracted from each crystal was detected by proportional counters, one for each crystal. The Fe XXI and Fe XXII lines were both observed with ADP crystal ($2d = 10.64$ Å). The ADP channel operated until the *SMM* spacecraft reentered the Earth's atmosphere in 1989 December, though the M4.5 flare on 1985 July 2 was the only occasion when the Fe XXI $2p^2$–$2p4l$ lines were observed. Having made some spatial scans, the last of which was around 21:11 UT when the flare had just begun,

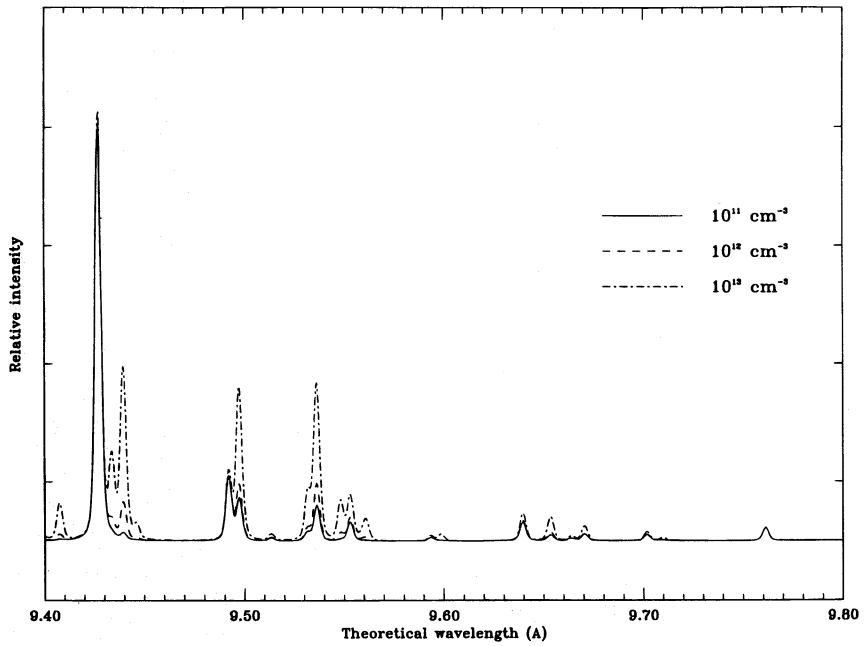

FIG. 2.—Synthetic spectra based on the intensity ratios of the Fe XXI lines in Table 2 in the range 9.4–9.8 Å. The plotting symbols used for the three electron densities are indicated. Line wavelengths are theoretical values.

TABLE 3

CALCULATED INTENSITIES OF Fe XXI $n = 2$–4, 5 X-RAY LINES

TRANSITION[a] (j–i)	THEORY WAVELENGTH (Å)	THEORETICAL INTENSITY RATIO[b]			
		$N_e = 10^{10}$ cm^{-3}	$N_e = 10^{11}$ cm^{-3}	$N_e = 10^{12}$ cm^{-3}	$N_e = 10^{13}$ cm^{-3}
22–1	9.5936	0.008	0.009	0.009	0.013
28–1	9.4271	1.000	1.001	1.005	1.032
42–1	8.5339	0.321	0.322	0.323	0.334
21–2	9.6639	0.006	0.006	0.007	0.011
23–2	9.5587	0.001	0.001	0.002	0.010
25–2	9.5134	0.007	0.007	0.008	0.015
26–2	9.4974	0.096	0.100	0.133	0.370
28–2	9.4921	0.154	0.155	0.155	0.159
30–2	9.4075	0.001	0.003	0.014	0.087
32–2	9.3952	0.003	0.005	0.020	0.117
33–2	9.3952	0.001	0.001	0.007	0.034
34–2	9.3947	0.002	0.002	0.008	0.055
40–2	8.5894	0.043	0.044	0.056	0.141
42–2	8.5871	0.047	0.047	0.047	0.049
46–2	8.5102	0.001	0.001	0.005	0.028
48–2	8.5057	0.002	0.002	0.008	0.041
49–2	8.5057	0.000	0.001	0.002	0.012
50–2	8.5055	0.001	0.001	0.003	0.019
22–3	9.7017	0.014	0.015	0.016	0.022
23–3	9.5987	0.002	0.002	0.004	0.017
25–3	9.5530	0.044	0.045	0.054	0.098
26–3	9.5368	0.008	0.009	0.012	0.032
27–3	9.5363	0.072	0.078	0.127	0.346
28–3	9.5315	0.015	0.015	0.015	0.015
30–3	9.4462	0.000	0.001	0.005	0.032
31–3	9.4396	0.006	0.015	0.088	0.408
32–3	9.4338	0.001	0.002	0.009	0.052
33–3	9.4338	0.003	0.005	0.026	0.132
38–3	8.6875	0.005	0.005	0.006	0.008
39–3	8.6273	0.021	0.021	0.025	0.044
40–3	8.6217	0.004	0.005	0.006	0.014
41–3	8.6205	0.029	0.031	0.050	0.133
46–3	8.5419	0.000	0.000	0.002	0.012
47–3	8.5396	0.002	0.005	0.028	0.129
48–3	8.5374	0.001	0.001	0.003	0.018
49–3	8.5373	0.001	0.002	0.009	0.044
24–4	9.7099	0.001	0.001	0.002	0.007
25–4	9.6704	0.016	0.017	0.020	0.036
26–4	9.6538	0.005	0.005	0.006	0.017
27–4	9.6533	0.009	0.009	0.015	0.042
30–4	9.5609	0.001	0.001	0.008	0.049
31–4	9.5542	0.000	0.000	0.003	0.013
32–4	9.5483	0.000	0.000	0.002	0.012
33–4	9.5482	0.002	0.003	0.016	0.080
35–4	9.5318	0.005	0.006	0.014	0.094
39–4	8.7229	0.006	0.006	0.007	0.012
41–4	8.7160	0.005	0.006	0.009	0.025
46–4	8.6356	0.000	0.001	0.003	0.017
49–4	8.6309	0.001	0.001	0.006	0.028
51–4	8.6250	0.002	0.002	0.006	0.037
28–5	9.7612	0.032	0.032	0.032	0.033
36–5	9.6396	0.046	0.046	0.049	0.067
42–5	8.8067	0.020	0.020	0.020	0.020
52–5	8.7139	0.021	0.021	0.023	0.031

[a] Level notation is that of Table 1.

[b] Intensities are relative to line $j = 28$ to $i = 1$ for $N_e = 10^{10}$ cm^{-3} and are in photon (not energy) units.

the FCS was commanded, by a programmed sequence, to do a wavelength scan over its entire range starting at 21:19 UT. Two Fe XXII line features, at 8.976 and 9.073 Å, were scanned at around 21:28 UT, very shortly after flare peak (see below), and the Fe XXI lines in the 9.4–9.8 Å range were scanned some minutes later, 21:32–21:35 UT. Figure 3 shows this portion of the spectrum. Note that the background emission is mostly instrumental, arising from the fluorescence of the crystals by solar hard X-ray emission, which declines with time and therefore wavelength (scanning is in the direction of increasing wavelength). The chief line features in Figure 3 are indicated by letters. Wavelengths and identifications, which will be discussed more fully in § 4.2, are given in Table 4. The absolute wavelengths from the ADP channel are, from the work of Phillips et al. (1982), likely to be accurate to 0.001 Å. From the lines observed in the 1985 July 2 flare in common with those discussed by Phillips et al., we estimate that there is no observable wavelength shift larger than 0.002 Å, giving an upper limit to any Doppler shifts of 60 km s^{-1}.

The BCS (Acton et al. 1980) operated during the entire flare duration. Its spectral range covered the He-like Fe

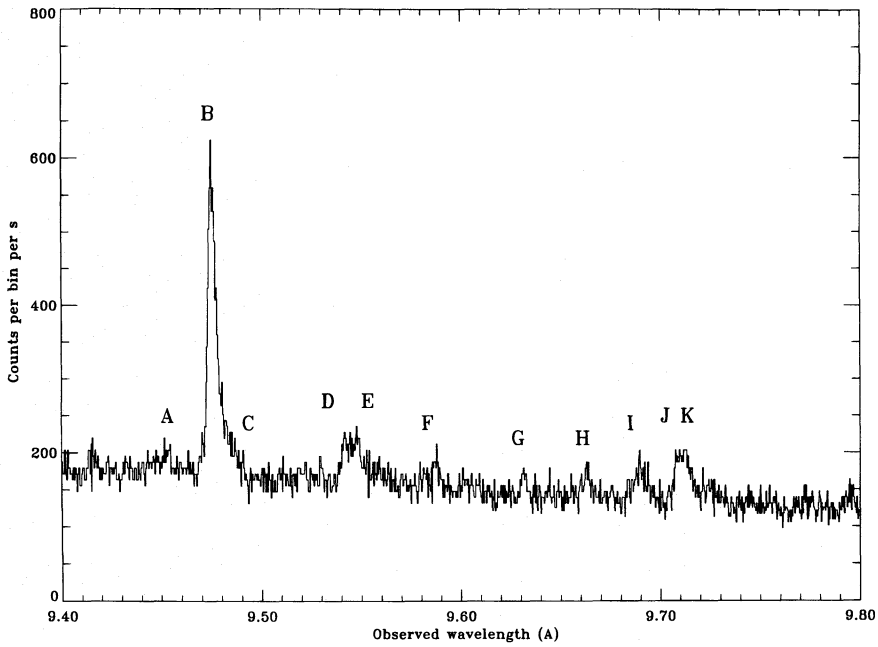

FIG. 3.—Portion of the FCS scan between 9.4 and 9.8 Å that includes the Fe XXI $2p^2$–$2p4l$ ($l = s, d$) lines discussed in the text (note background is mostly instrumental). Lines are identified by letters that are explained in the text and Table 4.

(Fe XXV) resonance line at 1.85 Å and satellites to the long-wavelength side, mostly formed by dielectronic recombination. These include Fe XXIV satellites and the density-sensitive Fe XX satellites at 1.90 Å. A further channel viewed the He-like Ca (Ca XIX) $1s^2$–$1s2l$ lines and Ca XVIII satellites. The Ca XIX resonance line flux peaked at 21:27 UT. The coarse collimator of the BCS, with 6′ FWHM field of view, limited the incident radiation to that from a single solar active region. As with the FCS, there is an instrumental background formed by crystal fluorescence, which imposes limitations on the use of the Fe XX lines as density indicators since near the maximum of large flares such as that on 1985 July 2 the lines are weaker than the background. Although spectra could be integrated in times as short as 11 s, it was found to be necessary to add spectra over longer periods to obtain statistical quality for comparison with theoretical spectra.

4. RESULTS

4.1. *Flare Temperature and Emission Measure*

The intensity of any of the dielectronically formed Fe XXIV satellites to that of the Fe XXV resonance line (line *w*, transition $1s^2\ ^1S_0$–$1s2p\ ^1P_0$) is a function of T_e, as

TABLE 4

COMPARISON OF OBSERVED AND THEORETICAL WAVELENGTHS AND INTENSITIES

	Observed Line			Nearest Fe XXI Line				
				Theory		Theory Intensity Ratio N_e		
Feature	Wavelength[a] (Å)	Identification[a]	Intensity Ratio[a]	Wavelength (+0.049 Å)	Identification[b]	10^{11} cm^{-3}	10^{12} cm^{-3}	10^{13} cm^{-3}
A.....	9.455	...	0.080	9.457	2–30	0.003	0.014	0.087
B.....	9.476	1–28	1.000	9.476	1–28	1.001	1.005	1.032
C.....	9.482[c]	3–31	0.163	9.489	3–31	0.015	0.088	0.408
D	9.542	2–28	0.138	9.541	2–28	0.155	0.155	0.159
E.....	9.548	2–30	0.146	9.546	2–26	0.100	0.133	0.370
F.....	9.587	3–27?	0.080	9.585	3–27	0.078	0.127	0.346
	...	...	$\lesssim$0.05[d]	9.602	3–25	0.045	0.054	0.098
G	9.632	1–22?	0.103	9.643	1–22[e]	0.001	0.001	0.002
H	9.663	Fe XIX	0.104	...	...	...	...	...
I.....	9.690	Fe XIX	0.306	9.689	5–36	0.046	0.049	0.067
J	9.709	Ne X	0.321	...	...	...	...	...
K	9.714	Fe XIX	0.302	...	...	...	...	...

NOTE.—Letters are from Fig. 3.

[a] Except for line feature A, from Fawcett et al. 1987, with estimated 10% uncertainties in intensities. Level notation is from Table 1. For feature A, wavelength and intensity are from best-fitting Gaussian profile to observed feature.

[b] From this work.

[c] Line on long-wavelength side of line B and also blended with Ne X 1*s*–5*p* (9.481 Å) line.

[d] No line observed; upper limit from eye estimate.

[e] The observed feature does not appear to be due to this Fe XXI transition (theoretical intensity too weak, wavelength difference too large), so another line probably contributes. It is possibly due to an Fe XIX line in the $2p^4$–$2p^3 5d$ array.

explained by Gabriel (1972). Satellite j (transition $1s^2 2p^2 P_{3/2}$–$1s2p^2\ ^2D_{5/2}$) is the most suitable for measurements with BCS spectra, being relatively free of line blends. In forming the intensity ratio, account must be taken of blended high-n satellites of the form $1s^2nl$–$1s2pnl$, which converge on the wavelength of the w line. Using the atomic data of Bely-Dubau et al. (1982) and using the spectral synthesis procedure described by Lemen et al. (1984), temperatures and emission measures were found throughout the duration of the flare under discussion here. This was also done for BCS Ca XIX spectra, though for such spectra satellite k (transition $1s^2 2p\ ^2P_{1/2}$–$1s2p^2\ ^2D_{3/2}$) was chosen. Figure 4 shows the temporal variations of integrated flux in the Fe XXV and Ca XIX w lines and electron temperature derived from the iron and calcium spectra. The error bars in these plots indicate count rate statistical uncertainties. As has been found on many previous occasions, the lower temperature Ca XIX flux peaks later (at 21:27 UT) than that of Fe XXV, reflecting the multithermal character of the flare plasma with a larger amount of hotter gas at flare peak than at later times. Also, as usual, the times of maximum temperature in each ion precede the peak flux by a few minutes.

4.2. *The* Fe XXI *Lines*

The most intense of the Fe XXI lines under discussion, at 9.476 Å (observed FCS wavelength, B in Fig. 3), is clearly identifiable with the 1–28 line of Fe XXI, theory wavelength 9.4271 Å. It is by far the strongest of the Fe XXI $n = 2$–4 lines, its large intensity being due to the fact that it is excited from the $2p^2\ ^3P_0$ ground level. This line was seen frequently throughout the lifetime of the instrument in second order in FCS channel 1 flare spectra on the short-wavelength side of the (unresolved) O VIII Lyα line pair at 18.970 Å.

Since the observed wavelengths are accurate to within 0.001 Å, the above comparison would suggest that the SUPERSTRUCTURE wavelengths are too small by 0.049 Å. Adding this amount to the theoretical Fe XXI wavelengths gives good agreement between the observed and calculated spectra in the wavelength range 9.455–9.587 Å, as can be seen from Table 4. The observed wavelengths and intensities are those given by Fawcett et al. (1987), who discuss this same flare. Thus, the observed intensity and wavelength of line D are consistent with the calculated values of the Fe XXI line 2–28, which does not vary appreciably with N_e. The observed intensity is a little smaller than the theoretical, but this is only just outside the estimated $\pm 10\%$ uncertainty of the observed intensities. This is in any case accounted for by the fact that the flare declined slightly over the 1 minute scan period from line B at 9.476 Å. The nearby line E is consistent with the Fe XXI line 2–26 if the value of N_e is around 2 or 3×10^{12} cm^{-3}. Line C is blended with line B on its long-wavelength side and is also coincident with the H-like neon (Ne X) $1s$–$5p$ line, which explains why the observed intensity is greater than the theoretical for $N_e \leq 10^{12}$ cm^{-3}. Line F is consistent with the Fe XXI line 3–27 at a density of 10^{11} cm^{-3} but no higher. If A is a real feature, it is accounted for by the Fe XXI 2–30 line, the measured intensity which has a 50% uncertainty being consistent with the calculated values for $N_e < 5 \times 10^{12}$ cm^{-3}. Although our calculations predict other Fe XXI lines at longer wavelengths, the observed line features appear to be mostly due to other ions, in particular Fe XIX lines in the $2p^4$–$2p^3 5d$ array.

Lines E and F are the best determinants of N_e, but as indicated there is an inconsistency in the value obtained. That from F is likely to be influenced by the fact that it was scanned 2 minutes after line B during the flare decline. Line E, however, is close in wavelength to line D, and so the relative intensities of these two lines should give a reliable value, suggesting that the higher value of N_e is correct. The rather uncertain measured intensity of line A supports this. In summary, the best estimate of N_e from the Fe XXI lines is 2 or 3×10^{12} cm^{-3}.

The consistency between observed and calculated spectra can be demonstrated further by comparing observed and synthetic spectra in the 9.45–9.6 Å range, which is done in Figure 5. The wavelength scale of the synthetic spectra is increased by 0.049 Å to match the observed spectrum. A uniformly sloping background has been subtracted from the observed spectrum, and the intensity scales are normalized. As can be seen, the synthetic spectrum calculated for $N_e = 10^{13}$ cm^{-3} gives a poor fit, so a density as high as this is ruled out. The relative intensities of lines D and E are best fitted by a theoretical spectrum, with N_e rather more than 10^{12} cm^{-3}.

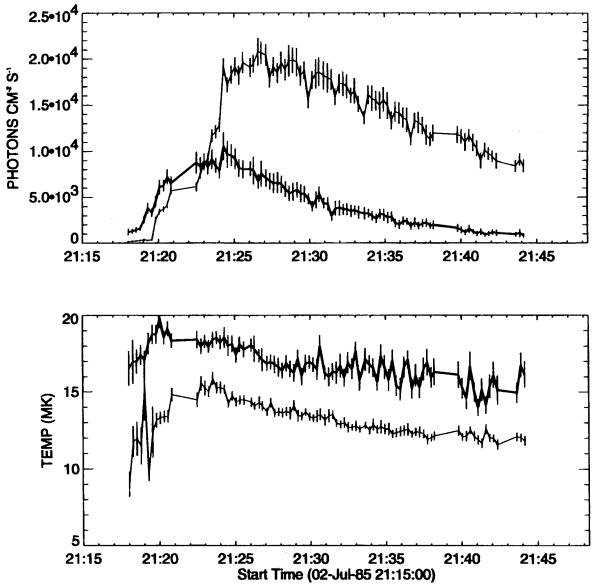

FIG. 4.—*Top*: Temporal variations of the integrated flux for the Ca XIX (*thin line*) and Fe XXV (*thick line*) resonance lines derived from synthetic spectral fits. *Bottom*: Temporal variations of the Ca XIX (*thin line*) and Fe XXV (*thick line*) electron temperatures deduced from synthetic spectral fits.

4.3. *The* Fe XXII *Lines*

As reported by Fawcett et al. (1987), two line features near 9 Å can be identified with Fe XXII transitions. That at 8.976 Å is due to $2p\ ^2P_{1/2}$–$4d\ ^2D_{3/2}$ (which we call line P), while a broader one at 9.073 Å is attributed to a blend of lines with transitions $2p\ ^2P_{3/2}$–$4d\ ^2D_{5/2}$ (line Q) and $2p\ ^2P_{3/2}$–$4d\ ^2D_{3/2}$ (line R). They are reasonably intense and not apparently blended with other lines (Fig. 6, *histogram*). Mason & Storey (1980), using the SUPERSTRUCTURE and distorted wave codes, calculate that line Q's intensity increases with N_e relative to line P. They give, for the intensity ratio $[I(Q) + I(R)]/I(P)$ as a function of N_e (cm^{-3}), the values 0.273 (10^{12}), 0.411 (10^{13}), and 1.05 (10^{14}). The

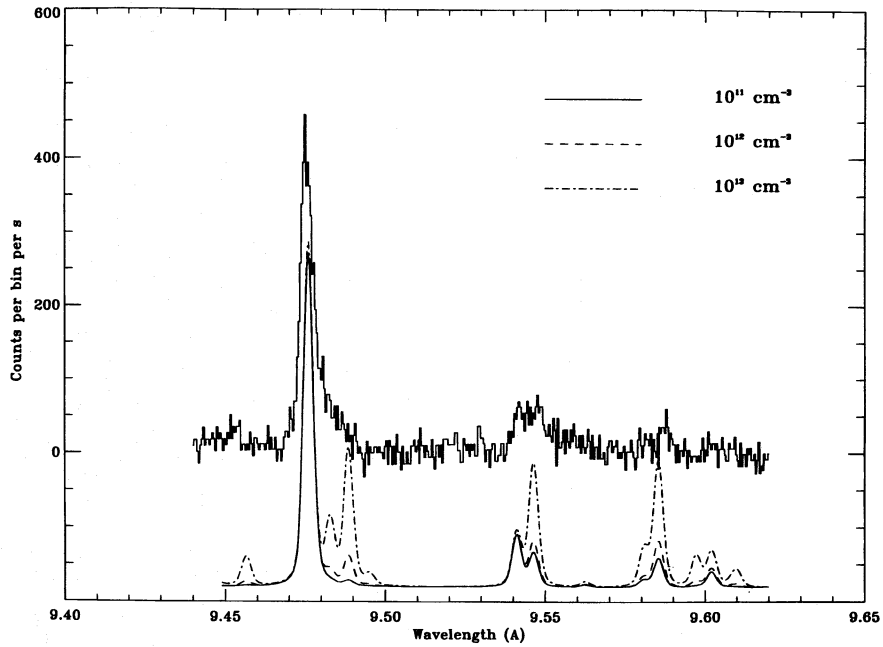

FIG. 5.—Observed spectrum (*histogram*) compared with calculated Fe XXI line spectra over the 9.4–10 Å range, displaced downward for clarity and converted to counts per FCS wavelength bin per second. A sloping background has been subtracted from the observed spectrum. The plotting symbols for the three electron densities in Fig. 2 are used here. Line features that are principally due to ions other than Fe XXI are indicated.

observed ratio from Fawcett et al. (1987) is 0.54 ± 0.03, the error range including both statistical uncertainties in the two line count rates and the background. This then suggests a very high electron density, of the order 10^{13} cm^{-3}. As with Fe XXI, the agreement between calculated and observed line intensities can be demonstrated with synthetic spectra. These are shown in Figure 6 for different densities based on Mason & Storey's calculations, the theoretical wavelengths having been slightly increased (as in the Fe XXI calculations), in this case by 0.06 Å.

Since the value of N_e implied by the Fe XXII lines is so high, even higher than the Mg XI density obtained by Linford & Wolfson (1988), it would be natural to question the validity of either the observed or calculated line intensities. However, we see no reason for doing this. The Fe XXII lines are as already stated unlikely to be blended with extraneous lines and are close in wavelength, so that large intensity variations are unlikely in the short (46 s) scan period over the 8.976–9.073 Å range. There does not seem to be any specific reason to doubt the calculations either, since

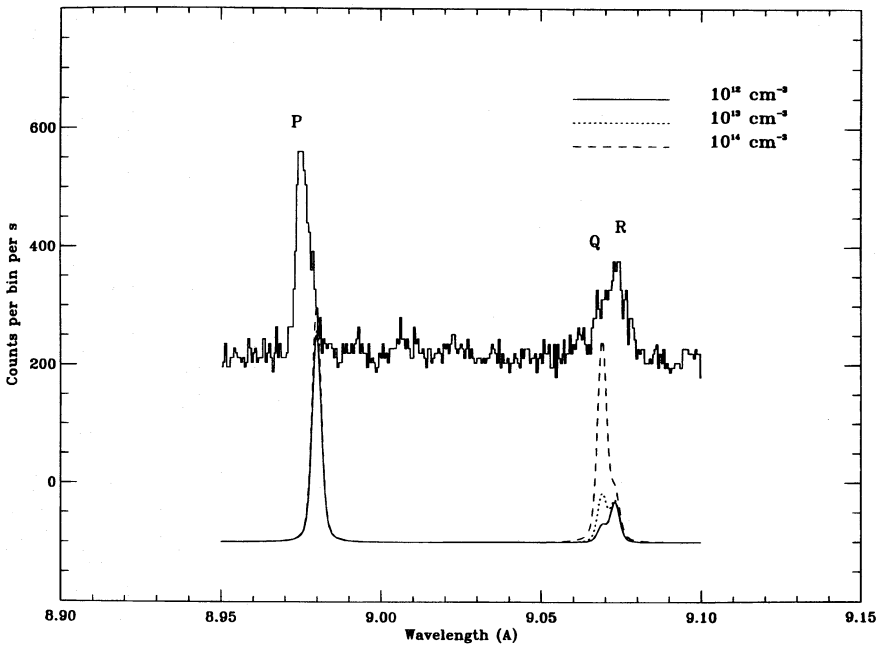

FIG. 6.—Observed spectrum (*histogram*) compared with calculated Fe XXII spectra over the 8.95–9.10 Å range, displaced downward for clarity. The plotting symbols used for the three electron densities are indicated.

Mason & Storey.'s collision strengths are in good agreement with other calculations and the derived intensities are in agreement with laboratory measurements.

4.4. *Inner Shell* Fe XX *Lines*

Further information about the electron density is available to us from the BCS, which observed Fe XX inner shell $1s$–$2p$ satellite lines about 1.90 Å. They are formed mostly from dielectronic recombination of C-like Fe ions and have a density dependence as discussed by Phillips et al. (1983). In the low-density ($N_e = 10^{11}$ cm^{-3}) limit, the several lines making up the $1s$–$2p$ array form two main line features, at 1.906 and 1.909 Å, with an intensity ratio of about 0.7:1. This ratio becomes 1.2:1 for $N_e = 10^{13}$ cm^{-3}.

The BCS observations near the peak of the 1985 July 2 flare show rather weak Fe XX line emission on a large background, though the Fe XXV line emission at this time is strong. Because of the weakness of the Fe XX lines, spectra were integrated over periods of 2 minutes to obtain improved statistical quality. The two main Fe XX line features are visible in such spectra over the period 21:22–21:40 UT, which includes the flare maximum in Ca XIX line emission and the times of the FCS Fe XXI and Fe XXII scans. The intensity ratio varies randomly with time between 0.50 and 0.72, with uncertainties of about 0.15, due to both statistical uncertainties in count rates and placing of the irregular instrumental background. The observed ratios, then, are consistent with that expected for a plasma in the low-density limit.

The apparent discrepancy between the electron densities near flare peak from FCS and BCS observations is explained by the widely different fields of view of the two instruments. The FCS was programmed to search for the brightest point in a 3′ × 3′ raster as soon as the flare was detected, followed by a 2′ × 2′ raster. With its 14″ × 14″ FWHM collimator, the FCS then performed the spectral scans. The BCS, on the other hand, was fixed in its position relative to the spacecraft, which was already directed at the active region in question at the start of the flare. The BCS collimator, 6′ × 6′ FWHM, included not only the flare emission but emission surrounding the FCS bright point, which is visible in the earlier FCS rasters preceding the spectral scans. The density upper limit implied by the BCS line ratios then refers to this extended region, whereas the FCS density estimates refer to the brightest point of the flare.

Much better flare imaging data are now available from the *Yohkoh* spacecraft. The *Yohkoh* soft X-ray telescope has a spatial resolution of better than 3″ at 8 Å, and the flare images it has obtained frequently show bright, confined loop-top sources (Acton et al. 1992; Feldman et al. 1994) as well as a more extended region consisting of the rest of the loop structure and sometimes other features as well. It seems likely that the FCS during the 1985 July 2 flare was directed to such a bright, loop-top source, which is thus associated with the large densities implied by the Fe XXII and Fe XXI line ratios. Meanwhile, the BCS observed more extended emission consisting of the remaining parts of the loop and surrounding regions and having a lower average density, $\leq 10^{11}$ cm^{-3}.

5. DISCUSSION

The Fe XXII and Fe XXI line ratios imply that the electron density of the emitting plasma viewed by the FCS was as high as 10^{13} cm^{-3} 1 minute after the flare peak (defined by the Ca XIX resonance line flux) and 2 or 3 × 10^{12} cm^{-3} about 5 minutes later. The Fe XXI and Fe XXII emission measures ($\sim 10^{49}$ cm^{-3}) imply emitting volumes that expand from 10^{23} to 10^{24} cm^3. We have no direct information about N_e late in the flare decay, e.g., around 21:45 UT (about 20 minutes after peak), but possibly we can use results for other flares (e.g., Phillips et al. 1982) suggesting $N_e \approx 10^{11}$ cm^{-3}. The rate of density decrease is then around $d \ln N_e/dt \approx 0.002$ s^{-1}. The Fe XXV and Ca XIX temperatures indicate a simultaneous cooling, which from Figure 4 is at an average rate of $dT_e/dt \approx -3 \times 10^3$ K s^{-1}.

The very small volumes of the emitting region implied by the Fe XXI and Fe XXII observations lead to tiny filling factors, which we calculate as follows. The FCS collimator views an area on the Sun which is 14″ square, or (10,200 km)^2. If we assume that the path length along the line of sight is also 10,200 km, then a volume of 1 × 10^{27} cm^3 is viewed by the FCS. The filling factor for the Fe XXII and Fe XXI volumes is thus 10^{-4} and 10^{-3}, respectively.

A very large magnetic field is required, at least near flare peak, to confine the hot plasma. Taking $N_e = 10^{13}$ cm^{-3} (from the Fe XXII lines) and $T_e = 10$ MK, i.e., a gas pressure $N_e kT_e$ of 14,000 dyn, a field strength of more than 500 G is needed to balance gas and magnetic pressures, while the corresponding field strength for $N_e = 2$–3×10^{12} cm^{-3} from the Fe XXI lines is 300 G. Though this is much larger than magnetic field strengths normally assumed for coronal flare loops, these values apply only to a confined structure within the loop geometry such as a small "knot" or thin current filament, as discussed below.

The value of N_e from the Fe XXII lines especially indicates an extremely short radiation cooling time. A measure of this is the time $\tau_{\rm rad}$ for a plasma to cool by a temperature ΔT_e, given by

$$\tau_{\rm rad} = \frac{3k\,\Delta T_e}{N_e \mathscr{R}(T_e)}\,, \tag{1}$$

where k is Boltzmann's constant and $\mathscr{R}(T_e)$ is the radiative power loss function. With $N_e = 10^{13}$ cm^{-3} and T_e to be the Fe XXV temperature at the time of the Fe XXII line scan, i.e., 17 MK, and using the calculation of Raymond, Cox, & Smith (1976) for $\mathscr{R}$, we find $\tau_{\rm rad}$ to be 1.4 s for $\Delta T_e = 1$ MK. Since the Fe XXV temperature declines at the rate of 1 MK per 300 s, a continuing energy input is implied.

More precisely, we may use the energy equation in the form

$$\mathscr{Q} = \frac{dU}{dt} + P_{\rm rad} + P_{\rm cond} \text{ ergs s}^{-1}\,, \tag{2}$$

where $\mathscr{Q}$ is the rate at which the hot plasma must be heated to maintain the observed X-ray emission, dU/dt is the rate of change of the total thermal energy of the plasma, and $P_{\rm rad}$ and $P_{\rm cond}$ are the energy loss rates due to radiation and conduction, respectively. We neglect any kinetic energy or enthalpy terms, since bulk motions are not indicated by FCS or BCS observations of any line shifts from the time of the flare peak onward. We put U, the total thermal energy of the plasma, equal to $3N_e kT_e V$ (V is the total volume of the plasma assumed to be in a loop geometry and with equal ion and electron densities). We assume classical (Spitzer-Härm) conductivity with a temperature gradient by T_e/L (L the semilength of the loop). Equation (2) then

becomes

$$\mathcal{Q} = 3N_e kT_e V\left(\frac{1}{T_e}\frac{dT_e}{dt} + \frac{1}{N_e}\frac{dN_e}{dt}\right) + N_e^2 V\mathcal{R}(T_e) + \frac{2A \times 10^{-6} T^{7/2}}{L}, \quad (3)$$

with A the loop's cross-sectional area (the factor 2 expressing the two loop footpoints). The second of the two terms in parentheses is much larger than the first if the above estimates of cooling and density decrease are used. A rough estimate of the conduction term may be obtained from the FCS image immediately before the crystal scan, which implies $L \approx 20{,}000$ km (A can be estimated from $V = 2AL$). It can be shown that the density decrease and conduction terms in equation (3) are of the same order and very small compared with the radiation loss term for the initial part of the flare decay. For these times, then, the energy input practically balances energy loss by radiation, which is equal to about 5×10^{26} ergs s^{-1}. If N_e is of order 10^{11} cm^{-3} in later stages, the radiation term becomes less important, and conductive loss is dominant.

The presence of very high densities at flare maximum indicated by this work and that of Linford & Wolfson (1988) raises issues for the wide range of models proposed to explain flare phenomenology. Thus, the idea of a pinched plasma that relaxes gradually during flare decay, advanced by Feldman et al. (1994) to explain impulsive flares seen by *Yohkoh*, fits in well with the high densities and very small emitting volumes derived here. If such emitting regions are at loop tops as discussed by Feldman et al. and Acton et al. (1992), the geometry is not looplike as assumed in equation (3), and cooling by conduction down to the chromosphere would not occur.

Of the flare models that have been developed recently, we will consider some consequences for the hybrid thermal/nonthermal model of Holman (1995) and Holman & Benka (1992). In this model, simultaneous Joule heating of the thermal plasma and runaway acceleration of electrons are produced by quasi-static electric fields that are aligned parallel to the loop magnetic field. The electric fields are maintained by currents that flow in filamentary sheets that are also aligned along the loop magnetic field. The high density derived from the Fe XXII observations allows us to place constraints on the thickness and number of these current sheets. In particular, the volume-integrated Joule heating produced by the current system is given by (Holman 1985)

$$Q_c = N_e kT_e V \nu_e \epsilon^2 \text{ ergs s}^{-1}, \quad (4)$$

where V is the heated volume. $\nu_e \approx 3.2 \times 10^2 N_e T_e^{-3/2}$ is the thermal collision frequency (for classical resistivity), and $\epsilon = E/E_D$ is the ratio of the electric field strength to the Dreicer field. The Dreicer field is the field strength at which all the electrons in the plasma undergo runaway acceleration. Substituting $Q = Q_c$ into equation (3) and using the volume of the Fe XXII emitting region for V, we solve for the value of ϵ required for current heating to sustain the observed soft X-ray emission at the time of maximum N_e. For $N_e = 10^{13}$ cm^{-3}, $T_e = 10^7$ K, and $V = 10^{23}$ cm^3, we obtain $\epsilon = 0.003$. Using equation (7) in Holman (1995), this small value of ϵ implies a correspondingly low electron collisional runaway rate $\dot{N} \ll 10^3$ s^{-1} The hard X-ray emission produced by these few electrons is negligible. The latter is consistent with *SMM* hard X-ray burst spectrometer observations that do not show any significant hard X-ray emission at the time of the first Fe XXII high-density measurement. We note that the derivation for ϵ is not sensitive to the choice of filling factor because the radiative cooling term dominates in the energy balance equation. In this case, $Q_c \approx P_{\text{rad}}$, and the product $N_e^2 V$ is effectively canceled.

We derive the thickness δr of individual sheets from the condition that the induction magnetic field of the current system cannot exceed the strength of the ambient loop magnetic field B. From Holman (1985), this condition for laminar sheets is expressed as

$$\delta r \lesssim 2.6 \times 10^{13} B\epsilon^{-1} T_e^{-1/2} N_e^{-1} \text{ cm}. \quad (5)$$

Substituting $B = 500$ G for the ambient field required to contain the heated plasma, and the derived ϵ, we obtain $\delta r \lesssim 160$ cm. We calculate the volume of each sheet according to $V_s = w_s L_s \delta r$, where w_s is the sheet width and L_s is the sheet length. Assuming that the sheet width scales as the emitting volume ($w_s \simeq V^{1/3}$), and equating the sheet length with the total loop length ($L_s \simeq 2L$), we deduce $V_s \lesssim 3 \times 10^{19}$ cm^{-3}. Finally, comparing the latter volume with the Fe XXII emitting volume, we infer $n_s \gtrsim 3 \times 10^3$ for the total number of current sheets.

It is encouraging to note that our inferred values of n_s and δr are similar to corresponding values derived by Benka & Holman (1994) for the 1980 June 27 flare from fits of hybrid thermal/nonthermal electron distributions to high-resolution hard X-ray spectra. An important difference between the latter results and the present calculation is the order-of-magnitude smaller value of ϵ, which is mainly a consequence of the much higher N_e derived from Fe XXII, and the requirement that the current heating rate balance the radiative cooling loss.

Part of this work was supported by NASA-RTOP grant 188-44-23-50. H. E. M. acknowledges support from the UK Particle Physics and Astrophysics Research Council, and D. M. Z. acknowledges support by NASA grant NAS 5-31235.

REFERENCES

Acton, L. W., et al. 1980, Sol. Phys., 65, 53
———. 1992, PASJ, 44, L71
Bely-Dubau, F., Dubau, J., Faucher, P., & Gabriel, A. H. 1982, MNRAS, 198, 239
Benka, S. G., & Holman, 1994, ApJ, 435, 469
Bhatia, A. K., Fawcett, B. C., Lemen, J. R., Mason, H. E., & Phillips, K. J. H. 1989, MNRAS, 240, 421
Burgess, A., & Sheorey, V. B. 1974, J. Phys. B, 7, 2403
Conlon, E. S., Keenan, F. P., & Aggarwal, K. M. 1992, Phys. Scripta, 46, 518
Eissner, W., Jones, M., & Nussbaumer, H. 1974, Comput. Phys., 8, 270
Eissner, W., & Seaton, M. J. 1972, J. Phys. B, 5, 2187
Fawcett, B. C., Jordan, C., Lemen, J. R., & Phillips, K. J. H. 1987, MNRAS, 225, 1013
Feldman, U., Hiei, E., Phillips, K. J. H., Brown, C. M., & Lang, J. 1994, ApJ, 421, 843
Gabriel, A. H. 1972, MNRAS, 160, 99
Gabriel, A. H., & Jordan, C. 1969, MNRAS, 145, 241
Holman, G. D. 1985, ApJ, 293, 584
———. 1995, ApJ, 452, 451
Holman, G. D., & Benka, S. G. 1992, ApJ, 400, L79
Kastner, S. O., & Bhatia, A. K. 1979, A&A, 71, 211
Lemen, J. R., Phillips, K. J. H., Cowan, R. D., Hata, J., & Grant, I. P. 1984, A&A, 135, 313

Linford, G. A., Lemen, J. R., & Strong, K. T. 1991, Adv. Space Res., 11(1), 147
Linford, G. A., & Wolfson, C. J. 1988, ApJ, 331, 1036
Loulergue, M., Mason, H. E., Nussbaumer, H., & Storey, P. J. 1985, A&A, 150, 246
Mason, H. E., Doschek, G. A., Feldman, U., & Bhatia, A. K. 1979, A&A, 73, 74
Mason, H. E., & Storey, P. J. 1980, MNRAS, 191, 631
McKenzie, D. L., Broussard, R. M., Landecker, P. B., Rugge, H. R., Young, R. M., Doschek, G. A., & Feldman, U. 1980, ApJ, 238, L43
Mewe, R., Gronenschild, E. H. B. M., & van den Oord, G. H. J. 1985, A&AS, 62, 197
Pallavicini, R., Serio, S., & Vaiana, G. S. 1977, ApJ, 223, 1058
Phillips, K. J. H., et al. 1982, ApJ, 256, 774
Phillips, K. J. H., Harra, L. K., Keenan, F. P., Zarro, D. M., & Wilson, M. 1993, ApJ, 419, 426
Phillips, K. J. H., Lemen, J. R., Cowan, R. D., Doschek, G. A., & Leibacher, J. W. 1983, ApJ, 265, 1120
Raymond, J. C., Cox, D. P., & Smith, B. W. 1976, ApJ, 204, 290
Saraph, H. E. 1972, Comput. Phys. Commun., 3, 256
Spicer, D. S. 1977, Sol. Phys., 53, 305
Spitzer, L. 1962, Physics of Fully Ionized Gases (2d ed.; New York: Wiley)
Underwood, J. H., Antiochos, S. K., Feldman, U., & Dere, K. P. 1978, ApJ, 224, 1017
Wolfson, C. J., Doyle, J. G., Leibacher, J. W., & Phillips, K. J. H. 1983, ApJ, 269, 319
Zarro, D. M., Mariska, J. M., & Dennis, B. R. 1995, ApJ, 440, 888